Tunnelling and Underground Space Technology 165 (2025) 106834

Contents lists available at ScienceDirect

Tunnelling and Underground Space Technology incorporating Trenchless Technology Research

journal homepage: www.elsevier.com/locate/tust

Blast loading prediction from methane-air explosion in long straight tunnels

Di Chen [a,b,c], Huaixin Zhang [a,*], Jun Li [c], Chengqing Wu [b,c,**]

[a] Computer Science School, Southwest Petroleum University, 610500 Chengdu, China
[b] Institute of Rock and Soil Mechanics, Chinese Academy of Sciences, Wuhan 430071, China
[c] School of Civil and Environmental Engineering, University of Technology Sydney, Sydney, NSW 2007, Australia

ARTICLE INFO

Keywords:
Gas explosion
Tunnel blast loading
CFD
Artificial neural network

ABSTRACT

Long, straight underground tunnels are vital to modern infrastructure, including resource extraction, transportation, and hydropower, but their confined nature heightens the risks posed by methane-air explosions. This study presents a dimensionless predictive model for evaluating blast loading resulting from methane-air explosions in long, straight tunnels, integrating numerical simulations, parametric analyses, and an artificial neural network (ANN)-based approach. By adopting dimensionless input and output parameters, the model becomes inherently scalable to various tunnel sizes and configurations, eliminating the influence of scale effects and ensuring a broad range of applicability. A validated CFD model using FLACS provided the database for the ANN training, capturing the transition from deflagration to shock wave formation as well as key pressure duration and magnitude characteristics. The ANN-based model, accounting for cross-sectional area and shape, tunnel length, fuel length, blockage ratio and obstacle spacing, demonstrated acceptable predictive capability with R^2 values above 0.95 and most predictions within a ± 30 % error margin. Validation against large-scale experiments confirmed its reliability and practicality. This model significantly reduces computational costs and time, offering an efficient tool for predicting methane-air explosion loads in underground tunnels.

1. Introduction

Long, straight underground tunnels play a critical role in modern infrastructure, including resource extraction, transportation, and hydropower (Tan, 2021; Cheng, 2021; Li, 2020). These confined environments ensure efficient connectivity and access. Despite their critical role, these confined spaces face significant risks, particularly from gas explosions. Methane (CH_4), commonly released in coal seams, organic deposits, and pipelines, poses a substantial hazard due to its flammability. Upon ignition, methane explosions generate intense overpressures and destructive shock waves, jeopardizing human safety and structural integrity.

The risks posed by methane explosions are well-documented in real-world incidents. For instance, in Taiwan's reservoir tunnel excavation projects, the ignition of combustible gases caused two fatalities and severe equipment damage (Li, 2020). Coal mines are especially vulnerable, with methane explosions accounting for 56 % of all accidents (Zhao, 2022; Zhang and Ma, 2015). Between 2000 and 2016, 232 large-scale mining disasters in China involved methane explosions, causing more than 10 fatalities per incident and representing 47.5 % of such events (Chen et al., 2013). Similarly, transportation tunnels have experienced catastrophic methane ignitions, with one incident causing 208 casualties (Li, 2018). These incidents underline the urgent need for robust methane-air explosion predictive models to guide safety measures in underground tunnels.

Predicting methane-air explosion loads inside tunnels is challenging due to the complex interplay of factors such as flow geometry, fuel concentrations, ignition locations, and varying boundary conditions. Existing studies have attempted to characterize overpressure evolution in underground environments (Uystepruyst and Monnoyer, 2015; Chen, 2024). However, these efforts often rely on case-specific empirical formulations or direct numerical simulations (Chen et al., 2023; Chen, 2024). While high-fidelity CFD tools like FLACS can capture detailed explosion dynamics (Hernandez, 2024; Chen, 2023), their resource demands hinder rapid assessments needed for emergency response or early-stage design optimization (Chen et al., 2025). Furthermore, traditional models often struggle to adapt to tunnels of varying scales and configurations, limiting their practicality (Zhang, 2023).

To address these limitations, dimensionless analysis has emerged as a promising approach. By transforming variables such as explosion

* Corresponding author at: Computer Science School, Southwest Petroleum University, 610500 Chengdu, China.
** Corresponding author at: Institute of Rock and Soil Mechanics, Chinese Academy of Sciences, Wuhan 430071, China.
E-mail addresses: zhxswpu@swpu.edu.cn (H. Zhang), chengqing.wu@uts.edu.au (C. Wu).

https://doi.org/10.1016/j.tust.2025.106834
Received 5 January 2025; Received in revised form 12 March 2025; Accepted 29 June 2025
Available online 8 July 2025

energy, distance, overpressure and impulse into dimensionless forms, researchers can generalize results across configurations. For example, the multi-energy model effectively employs dimensionless parameters to analyze blast behavior under diverse conditions in unconfined conditions (van den Berg, 1985). This generalization enhances adaptability and reduces computational effort by enabling a single dimensionless framework to represent multiple physical scenarios.

Machine learning (ML), particularly ANNs, further advances predictive capabilities by modeling complex, nonlinear relationships in explosion scenarios. ANNs have been used to estimate peak pressures and impulses at various tunnel locations (Zhang, 2023; Xu, 2023; Grégoire, 2022; Chen, 2022). However, many existing ANN-based models lack dimensionless formulations, limiting their scalability.

This study aims to develop a scalable, efficient, and accurate predictive tool for methane-air explosion-induced loads in long, straight tunnels. By integrating dimensionless analysis with ANN modeling, the proposed framework overcomes the limitations of existing approaches. Validated CFD simulations provide a robust dataset, which is transformed into dimensionless parameters for ANN training. The resulting model not only predicts key blast characteristics but also adapts to various tunnel sizes and configurations. This practical tool bridges the gap between high-fidelity simulations and real-world applications, enhancing safety and resilience in underground tunnels.

2. Numerical model and validation

2.1. Introduction to the numerical code

In this study, the FLACS computational fluid dynamics (CFD) toolbox was employed to analyze the dynamics of methane-air explosions in a long, straight tunnel. FLACS utilizes a three-dimensional mesh and finite-difference methods to solve the conservation equations for compressible fluids (GEXCON, 2019). What distinguishes FLACS from many other commercial CFD codes is its innovative concept of distributed porosity, which is particularly well-suited for modeling complex flow geometries. This capability enables efficient computations for industry-scale simulations, even on personal computers. This method incorporates large obstacles directly into the computational grid, while smaller objects (those smaller than the mesh size) are represented in a sub-grid using specialized models. These sub-grid models address flow resistance, turbulence, and flame wrinkling caused by the smaller objects. This distinctive feature makes FLACS an effective tool for performing full-scale gas explosion simulations.

2.2. Numerical model validation

Numerical model was developed using the FLACS to investigate the methane-air explosion loading in long straight tunnels. The numerical model was validated using full-scale experimental data from a 710-meter-long tunnel, as presented in the authors' previous study (Chen, 2024). The experimental setup, as shown in Fig. 1 and Fig. 2, consisted of a long, straight tunnel with one sealed end and the other open to the surrounding air. The tunnel measured 3.2 m × 2.6 m in cross-section and had a total length of 710 m.

The initial 28 m near the sealed end was filled with 9.5 % (V) methane-air mixture, with a total volume of approximately 200 m^3. The ignition point was located near the sealed end, and obstacles were distributed along the tunnel. Two repeated tests were conducted, during which overpressure was measured along the tunnel's lateral wall, extending up to 100 m from the closed end.

As shown in Fig. 2, the obstacle distribution near the sealed end of the tunnel was modeled in detail. A mesh size of 0.2 m, previously validated for large-scale tunnel simulations (Zhang, 2023), was adopted. Time-step control parameters based on the Courant-Friedrich-Levy (CFL) number, namely CFLC = 5 and CFLV = 0.5, were employed to balance computational efficiency and accuracy. These parameters, as recommended in the FLACS user manual (GEXCON, 2019), allowed the blast wave and fluid to propagate by 5 and 0.5 times the grid length, respectively, during each time step.

To improve the accuracy of far-field blast predictions, the STEP="KEEP_LOW" option was activated (Hansen and Johnson, 2015). This setting prevented time steps from increasing as the explosion subsided, reducing numerical smearing of the blast waves. The computational domain was extended by 100 m beyond the open end of the tunnel to mitigate boundary effects, and a none-reflecting boundary condition ("PLANE_WAVE") was applied at the direction of open end to prevent blast wave reflection at the outer boundary. Reflective boundary conditions (Euler) were used for the other walls. Heat loss through radiation, conduction, and convection was incorporated using the "RADIATE = 04" setting and the heat_switch keyword. A wall function was activated to handle shear forces near the wall regions. Ambient conditions were set at 20 °C and 1 bar.

Fig. 3 presents a comparison of overpressure history curves obtained from simulations and experiments along the tunnel. Up to 60 m from the ignition point, the overpressure exhibited a deflagration pattern (Chen, 2024), characterized by a relatively gradual increase followed by pressure decay. Beyond 80 m, the pressure wave transformed into a shock wave, marked by a sharp pressure rise (Bjerketvedt et al., 1997).

Although some discrepancies between the experimental and numerical results were observed, these can be attributed to inherent

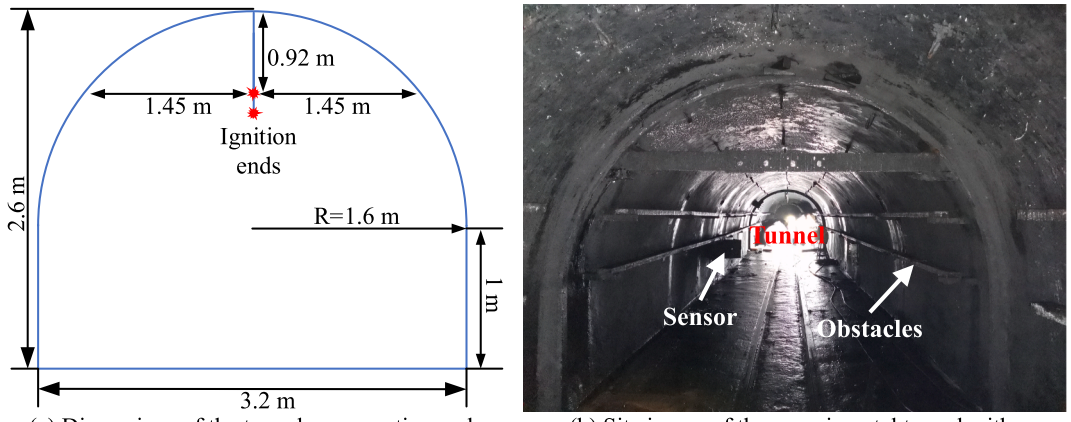

(a) Dimensions of the tunnel cross section and ignition point location

(b) Site image of the experimental tunnel with obstacles

Fig. 1. Dimensions and site image of the experimental tunnel.

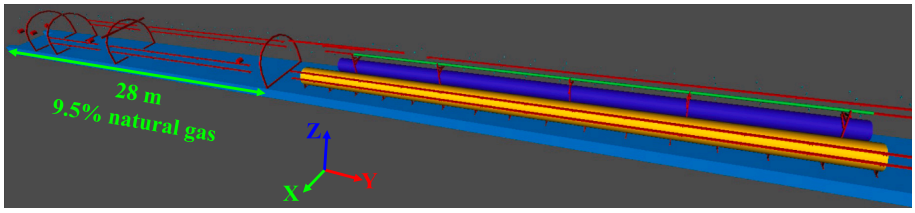

Fig. 2. Obstacle distribution along the tunnel.

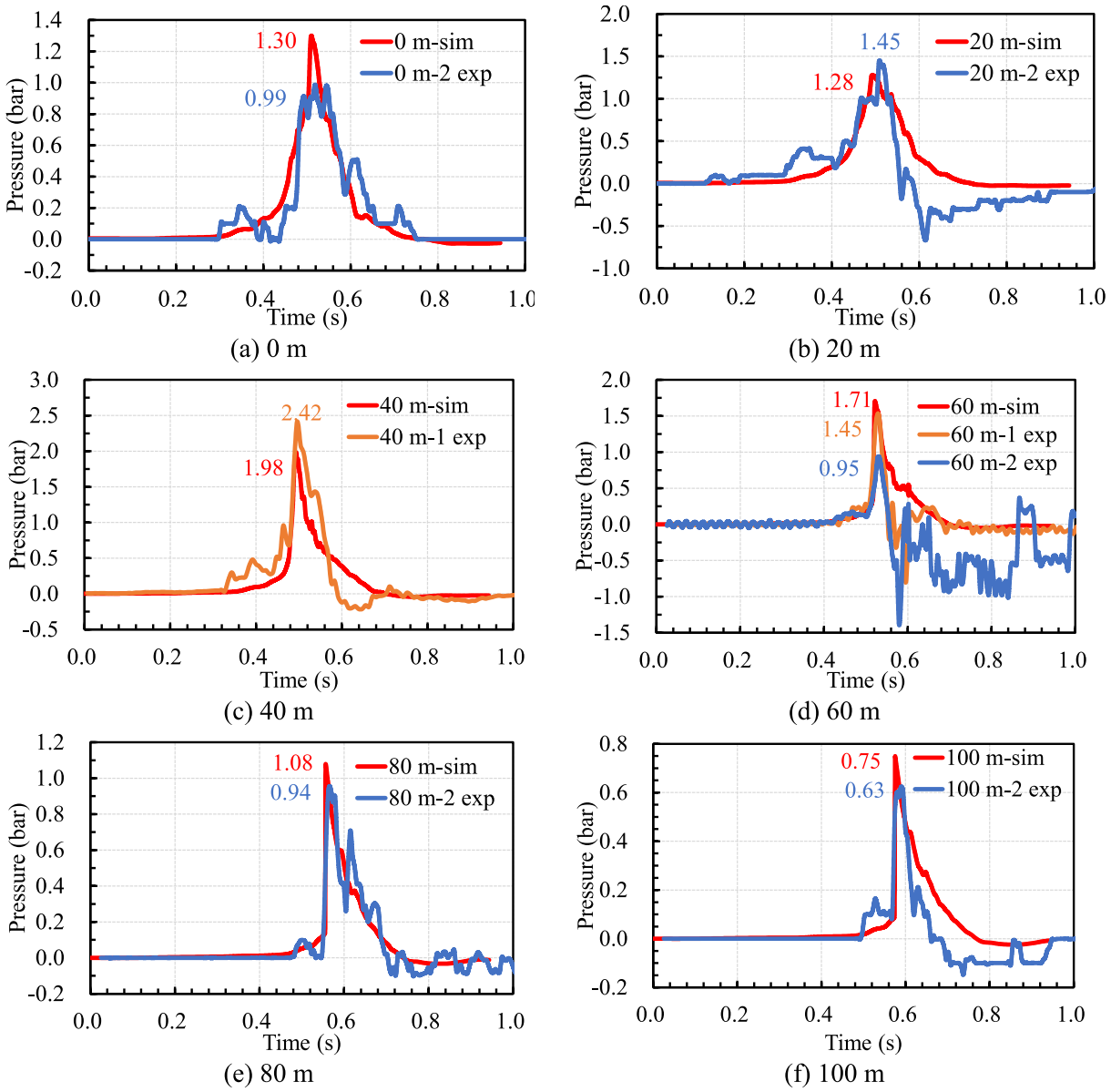

Fig. 3. Overpressure history comparison at different distances.

experimental uncertainties, such as variations in humidity and wall roughness, which are difficult to model precisely. Nevertheless, the numerical model effectively captured the key characteristics of the deflagration and shock waves, accurately replicating both pressure duration and magnitude.

In summary, despite some extent of inconsistencies, the validation demonstrated that FLACS provides reliable predictions of gas explosion loads in large-scale tunnels, both in the near and far fields.

3. Effects of key parameters on gas explosion loads in tunnels

3.1. Physical models

Seven sets of physical models were established to investigate the impact of various key parameters on the loading characteristics of methane-air mixture explosions in long straight tunnels. These parameters include ignition position, cross-sectional area, tunnel length, cross sectional shape, fuel length, blockage ratio, and obstacle distance, and

their ranges are shown in Table 1. It is widely recognized that the stoichiometric concentration of a fuel–air mixture is linked with the most severe consequences for vapor cloud explosions (Bjerketvedt et al., 1997), with the stoichiometric concentration for methane-air mixture being 9.5 % (V). Following a similar approach to the development of the multi-energy model (van den Berg, 1985), and prioritizing the worst-consequence scenario, the homogeneous methane-air mixture with stoichiometric concentration was selected for the following model.

Fig. 4 illustrates a generic physical model to help describe the models in this section. One end of the tunnel was closed, while the other end remained open to the surrounding air. The height and width of the tunnel were denoted as H and W, respectively. The closed end of the tunnel was filled with 9.5 % methane-air mixture, with a length of L_{fuel}. The tunnel wall was modeled as rigid with a straight shape in length, and a thickness of 0.8 m. Obstacles were placed at the bottom of the tunnel to mimic congestions. These obstacles were also modelled as rigid with a distance of D_{obstacle}. Obstacles were constructed with rectangular cross-sections because sharp-edged obstacles aligned with the main flow direction have been observed to lead to more pronounced flame front distortion and, consequently, more severe consequences (Xu et al., 2020). A cuboid mesh with a grid size of 0.2 m was employed, and the computational domain was extended sufficiently to minimize boundary effects. The initial temperature and pressure were 20 ℃ and 1 bar, respectively. Monitors were placed at the center of the cross-sectional area, spaced of 10 m apart, to capture the blast parameters, such as overpressure and impulse. The detailed parameters were introduced in the following corresponding sections.

3.2. Effect of ignition position

This section investigated the influence of ignition positions on blast loading in a 1000-meter-long tunnel with a square cross-section of 4 m × 4 m. The fuel, distributed along a 50-meter segment of the tunnel, was ignited at five specific positions: 0 m, 12.5 m, 25 m, 37.5 m, and 50 m from the closed end. To simulate congestion within the tunnel, obstacles were placed along the bottom center of the cross-section. These obstacles, measuring 2.4 m in width, 0.4 m in thickness, and 0.4 m in height (blockage ratio, $BR = 0.06$), were spaced 8 m apart.

Firstly, the overpressure distribution within each cross-section was analyzed to confirm whether it exhibits a one-dimensional (1D) distribution. Overpressure data were recorded at the start (0 m), middle (500 m), and end (1000 m) cross-sections of the tunnel during the simulation. For each cross-section, measurements were taken at nine evenly spaced points. As shown in Fig. 5, the overpressure values within the same cross-section were nearly identical, with minimal variation across the points. This near overlap of data points indicates that the overpressure was uniformly distributed within each cross-section. Consequently, overpressure can be approximated as a 1D distribution, varying primarily with time and distance along the tunnel's longitudinal axis. Therefore, in the following parts, the overpressure data was taken from the center of the cross section.

Additionally, it can be noted that the pressure duration inside the tunnel spanned several seconds, which is substantially longer than the typical durations of a few hundred milliseconds observed in normal gas explosions (Bjerketvedt et al., 1997).

Fig. 6 illustrates the peak pressure and impulse comparison under different ignition locations. Both metrics decreased as the ignition position moved further from the closed end (0 m) toward the fuel end (50 m). For ignition at the fuel end, the peak pressure was less than 10 kPa, insufficient to cause significant structural damage or human casualty (Zhu, 2020).

This trend can be attributed to the completion of pressure build-up and venting. Igniting at the closed end traps combustion products, enhancing pressure buildup. As the ignition shifts towards the open end, combustion products expand freely, reducing overpressure. When ignited at the fuel end, the products expand into the entire tunnel, minimizing pressure buildup. Consequently, the overpressure for this case was significantly lower as compared to others (Bjerketvedt et al., 1997).

3.3. Effect of cross-sectional area

This section investigated the effect of cross-sectional areas on blast loading in a 1000-meter-long tunnel. The fuel, distributed along a 50-meter section at the closed end (0 m), was ignited to ensure maximum blast loading. Three cross-sectional areas were analyzed: 2 m × 2 m, 4 m × 4 m, and 8 m × 8 m. To maintain a consistent blockage ratio of 0.06, obstacle dimensions were adjusted as follows: 0.6 m × 0.4 m × 0.4 m (width × thickness × height) for the 2 m × 2 m section, 2.4 m × 0.4 m × 0.4 m for the 4 m × 4 m section, and 4.8 m × 0.4 m × 0.8 m for the 8 m × 8 m section. Obstacles were spaced 8 m apart.

Fig. 7 illustrates the comparison of peak pressure and impulse under different cross-sectional areas. The 2 m × 2 m section exhibited the highest peak pressure within the first 250 m of the tunnel, nearly double that of the 4 m × 4 m and 8 m × 8 m sections. However, its peak pressure declined much faster beyond 250 m, dropping to about half the value of the larger sections at the 1000-meter mark. In contrast, the 4 m × 4 m and 8 m × 8 m sections showed comparable peak pressures throughout the tunnel length. The impulse for the 2 m × 2 m section was higher than that of the other two sections up to 400 m but dropped rapidly and fell below the impulse values of the 4 m × 4 m and 8 m × 8 m sections after 600 m. These trends can be attributed to the confined nature of smaller cross-sectional areas, which restrict the dispersion of combustion products and result in higher initial overpressures. However, this confinement also accelerates pressure dissipation along the tunnel. Conversely, larger cross-sectional areas allow greater expansion of combustion products, mitigating peak pressures but sustaining impulse over longer distances. This highlights the significance of tunnel dimensions in influencing the propagation and attenuation of explosion loads.

Table 1
Variables and their ranges for parametric study, the length dimension is meter.

NO.	Variables	Ranges	Ignition position	Cross-sectional area	Tunnel length	Cross-sectional shape	Fuel length	Blockage ratio	Obstacle distance
1	Ignition position	Closed end, 1/4, 2/4, 3/4, other end	/	4 × 4	1000	4 × 4	50	0.06	8
2	Cross-sectional area	2 × 2, 4 × 4, 8 × 8	Closed end	/	1000	4 × 4	50	0.06	8
3	Tunnel length	1000, 600, 400, 200	Closed end	4 × 4	/	4 × 4	50	0.06	8
4	Cross-sectional shape	2 × 8, 3.2 × 5.2, 4 × 4, 5.2 × 3.2, 8 × 2	Closed end	4 × 4	1000	/	50	0.06	8
5	Fuel length	5, 10, 30, 50	Closed end	4 × 4	1000	4 × 4	/	0.06	8
6	Blockage ratio	0.20, 0.10, 0.06, 0.02	Closed end	4 × 4	1000	4 × 4	50	/	8
7	Obstacle distance	12, 8, 4	Closed end	4 × 4	1000	4 × 4	50	0.06	/

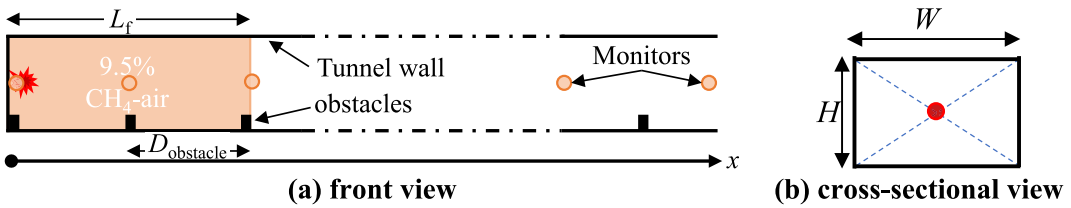

Fig. 4. Generic physical model for the parametric study.

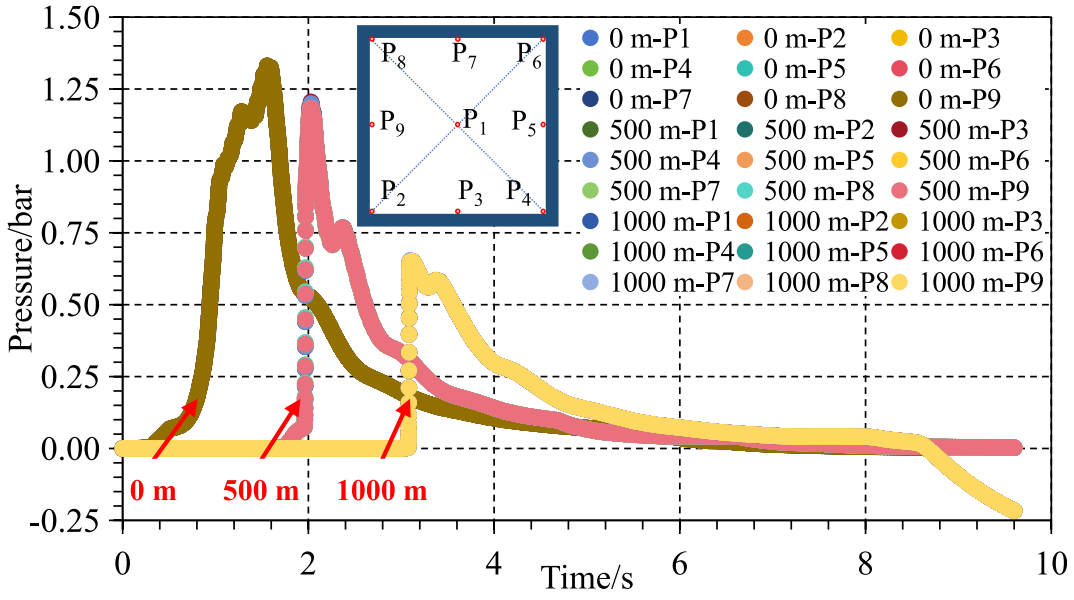

Fig. 5. The overpressure distribution at the cross sections of the start (0 m), middle (500 m), and end (1000 m) of the tunnel.

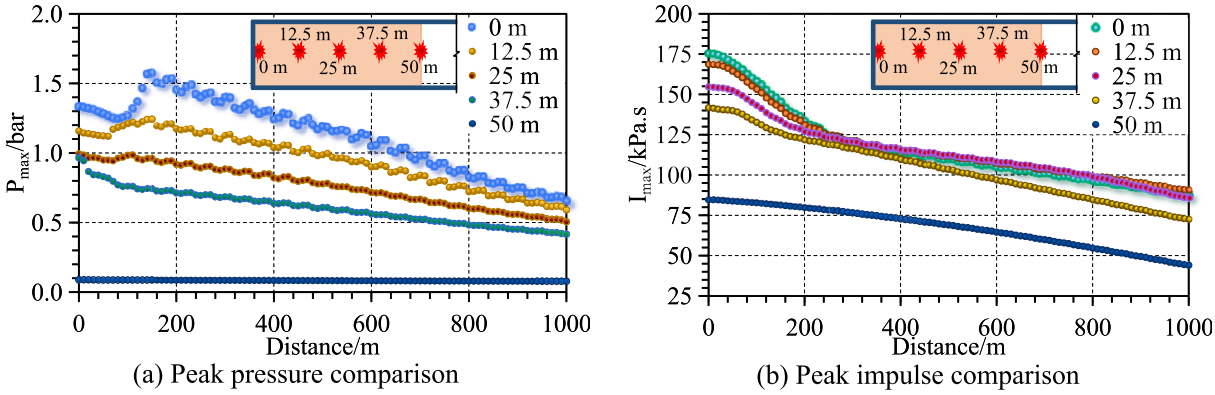

Fig. 6. Peak pressure and impulse comparison with different ignition positions.

3.4. Effect of tunnel length

This section examined the influence of tunnel length on blast loading in tunnels with lengths of 1000 m, 600 m, 400 m, and 200 m. The cross-sectional dimensions of the tunnels were fixed at 4 m × 4 m. Other parameters, including fuel length, ignition position, obstacle size, and spacing, were identical to those used in the previous section.

Fig. 8 illustrates the comparison of peak pressure and impulse for different tunnel lengths. The results indicate that tunnel length had a negligible effect on the blast loading within the tunnel. Across all scenarios, the peak pressure and impulse values overlapped, demonstrating consistent blast characteristics regardless of the tunnel length. This outcome suggests that the propagation and attenuation of blast waves are largely independent of tunnel length under the given initial conditions.

3.5. Effect of cross-sectional shape

This section investigates how the cross-sectional shape of a 1000-meter-long tunnel affects blast loading. A shape factor $S_f = W/H$ was defined. Tunnels with $S_f < 1$ are considered slender, while those with $S_f > 1$ are classified as flat. Five different cross-sectional dimensions were examined: 2 m (W) × 8 m (H) ($S_f = 0.25$), 3.2 m × 5.2 m ($S_f = 0.62$), 4.0 m × 4.0 m ($S_f = 1.00$), 5.2 m × 3.2 m ($S_f = 1.63$), 8 m × 2 m ($S_f = 4.00$). The ignition was placed at the closed end, and the fuel length was fixed at 50 m. Obstacles were spaced every 8 m throughout the tunnel.

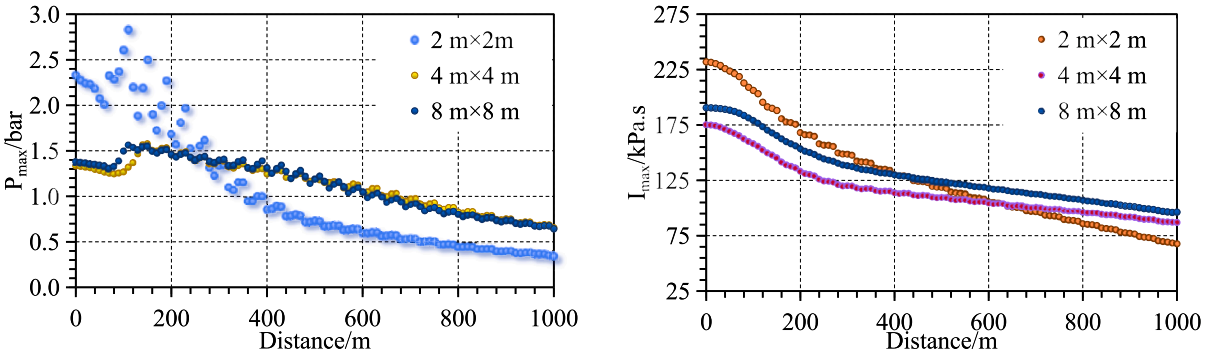

Fig. 7. Peak pressure and impulse comparison with different cross-sectional areas.

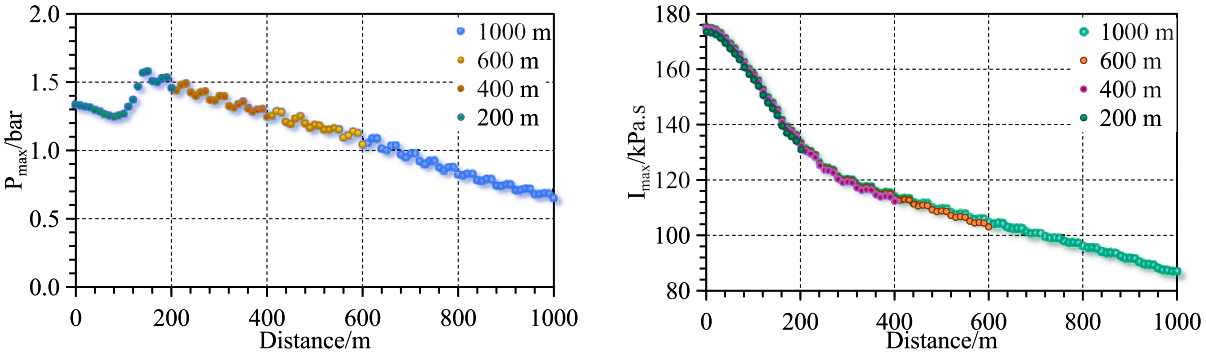

Fig. 8. Peak pressure and impulse comparison with different tunnel lengths.

Under a blockage ratio (*BR*) of 0.2, where $BR = A_{obstacle}/A_{tunnel}$ ($A_{obstacle}$ and A_{tunnel} are the respective cross-sectional areas of the obstacle and tunnel), the obstacle dimensions were scaled accordingly. As illustrated in Fig. 9, when S_f varied from 0.25 to 4.00, the influence of cross-sectional shape on blast loading exhibited a nonmonotonic trend. At the first 100 m from the ignition point, the 3.2 m × 5.2 m tunnel (S_f = 0.62) produced the highest peak pressure (4.8 bar), followed by the 5.2 m × 3.2 m (S_f = 1.63), 4.0 m × 4.0 m (S_f = 1.00), 8 m × 2 m (S_f = 4.00), and 2 m × 8 m (S_f = 0.25) configurations. With increasing distance, blast loading in the 5.2 m × 3.2 m tunnel diminished most rapidly, whereas the 2 m × 8 m tunnel retained comparatively higher pressures and impulses at 1000 m.

A similar examination was conducted at a *BR* of 0.06 (Fig. 10). Under this reduced blockage ratio, the obstacle dimensions were rescaled, and the 8 m × 2 m (S_f = 4.00) tunnel recorded the highest initial peak pressure (1.7 bar), albeit with the lowest impulse. The order of initial peak pressures then progressed through the 4.0 m × 4.0 m (S_f = 1.00), 5.2 m × 3.2 m (S_f = 1.63S), 2 m × 8 m (S_f = 0.25), and 3.2 m × 5.2 m (S_f = 0.62) configurations. As distance increased, the 8 m × 2 m configuration's blast loading attenuated rapidly, while the 2 m × 8 m tunnel retained elevated blast loading levels over a longer distance.

These observations highlight that cross-sectional shape substantially affects the distribution and attenuation of blast loads along the tunnel. The relationship is not strictly linear or monotonic, reflecting the

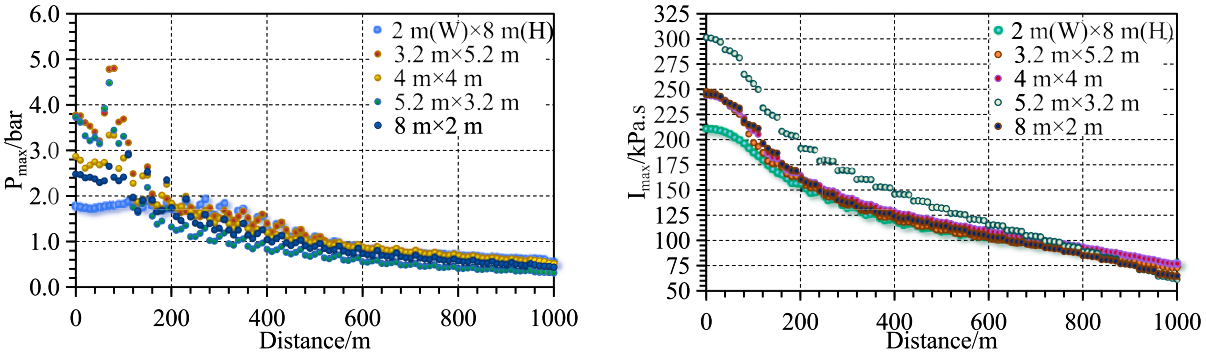

Fig. 9. Peak pressure and impulse comparison with different cross-sectional shapes (*BR* = 0.2).

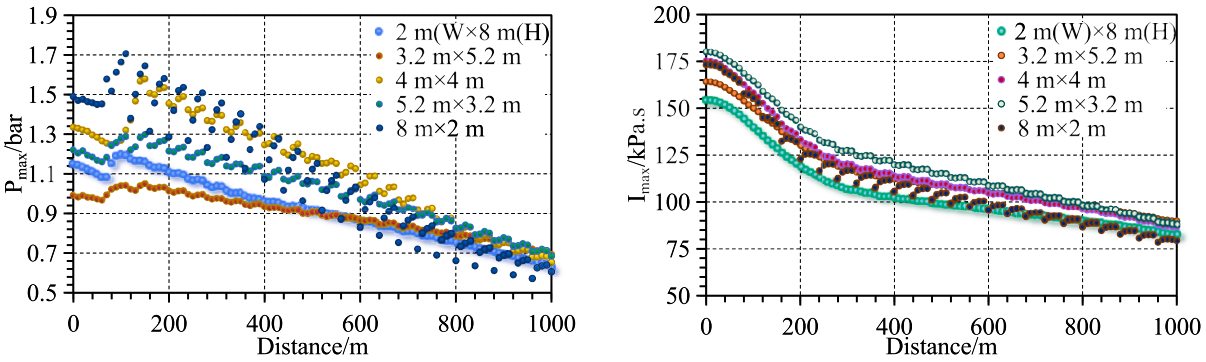

(a) Peak pressure comparison (b) Peak impulse comparison

Fig. 10. Peak pressure and impulse comparison with different cross-sectional shapes ($BR = 0.06$).

complex interplay between cross-sectional geometry, obstacle placement, flame propagation, and turbulent mixing.

3.6. Effect of fuel length

This section investigated the influence of fuel length on blast loading in a 1000-meter-long tunnel with a square cross-section measuring 4 m × 4 m. The fuel lengths considered were 5 m, 10 m, 30 m, and 50 m. Other parameters, such as tunnel length, ignition position, obstacle size, and spacing, were kept constant as in the previous sections.

Fig. 11 depicts the comparison of peak pressure and impulse across different fuel lengths. The results show a clear trend: as the fuel length increased from 5 m to 50 m, both the peak pressure and impulse significantly increased. Specifically, the maximum peak pressure and impulse exhibited nearly a fourfold rise as the fuel length increased. This suggests that longer fuel lengths release greater energy, leading to more intense blast loads.

3.7. Effect of blockage ratio

This section explored the effect of blockage ratio on blast loading in a 1000-meter-long tunnel with a square cross-section of 4 m × 4 m. The blockage ratios examined were 0.02 (obstacle size: 0.8 m × 0.4 m × 0.4 m), 0.06 (obstacle size: 2.4 m × 0.4 m × 0.4 m), 0.10 (obstacle size: 4.0 m × 0.4 m × 0.4 m), and 0.20 (obstacle size: 4.0 m × 0.4 m × 0.8 m). The fuel length was set at 50 m, and other parameters, such as tunnel length and ignition position, remained consistent with previous sections.

Fig. 12 compares the peak pressure and impulse for different blockage ratios along the tunnel. Near the closed end, both the peak pressure and impulse increased as the blockage ratio rose. This behavior is attributed to the intensified blast generation caused by enhanced turbulence and accelerated combustion due to higher blockage. However, as the distance from the closed end increased and approached the open end of the tunnel, both the peak pressure and impulse declined for higher blockage ratios. This phenomenon can be explained by the increased energy dissipation resulting from the enhanced turbulence caused by higher blockage, which leads to greater energy loss as the blast propagates through the tunnel. These results indicate that while higher blockage ratios intensify the initial blast effects, they also contribute to faster energy attenuation along the tunnel length.

3.8. Effect of obstacle distance

This section investigated how obstacle spacing affects blast loading in a 1000-meter-long tunnel with a square cross section of 4 m × 4 m. Three obstacle distances were considered: 4 m, 8 m, and 12 m. Four blockage ratios ($BR = 0.02$, 0.06, 0.1, and 0.2) were examined, while all other parameters remained consistent with those described in previous sections.

Fig. 13 compares peak pressure and impulse for different obstacle distances at $BR = 0.02$. As obstacle spacing increased, the peak pressure also increased, whereas the peak impulse remained nearly unchanged. This trend can be attributed to the influence of obstacles on blast formation. A closer obstacle arrangement intensifies turbulence and flame acceleration, thereby elevating local overpressure levels. However, since the total energy release from the explosion remains constant, scenarios with higher peak pressures are associated with shorter pressure durations. Consequently, the impulse, which integrates pressure over time, does not exhibit significant variation across different obstacle distances.

Fig. 14 shows the peak pressure and impulse at $BR = 0.06$. In this

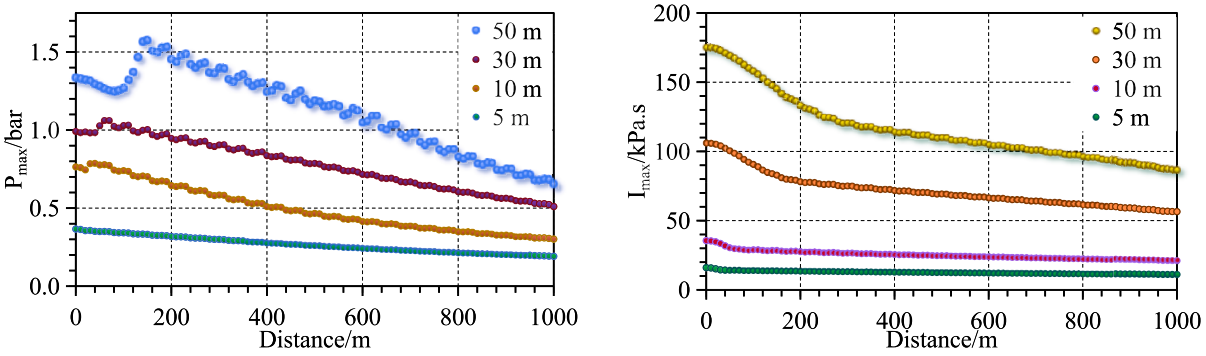

(a) Peak pressure comparison (b) Peak impulse comparison

Fig. 11. Peak pressure and impulse comparison with different fuel lengths.

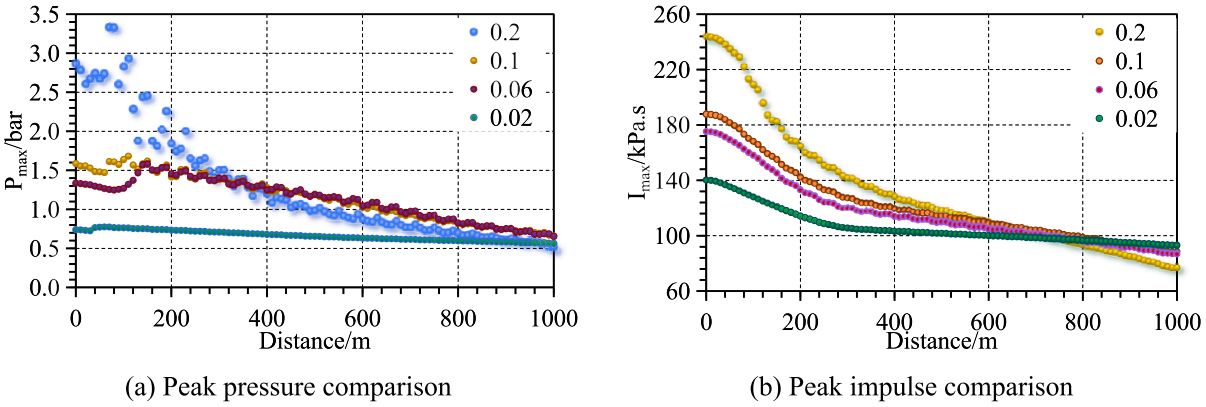

Fig. 12. Peak pressure and impulse comparison with different blockage ratios.

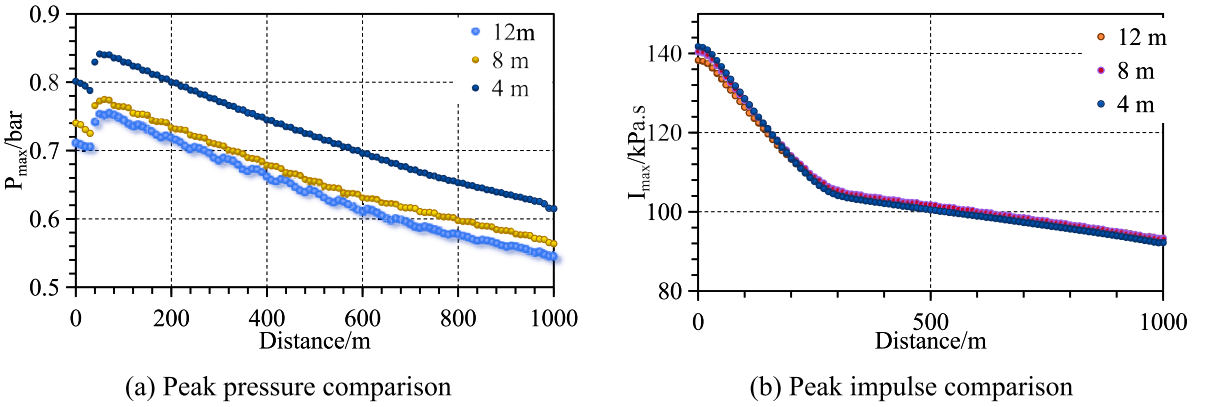

Fig. 13. Peak pressure and impulse comparison for different obstacle distances (BR = 0.02).

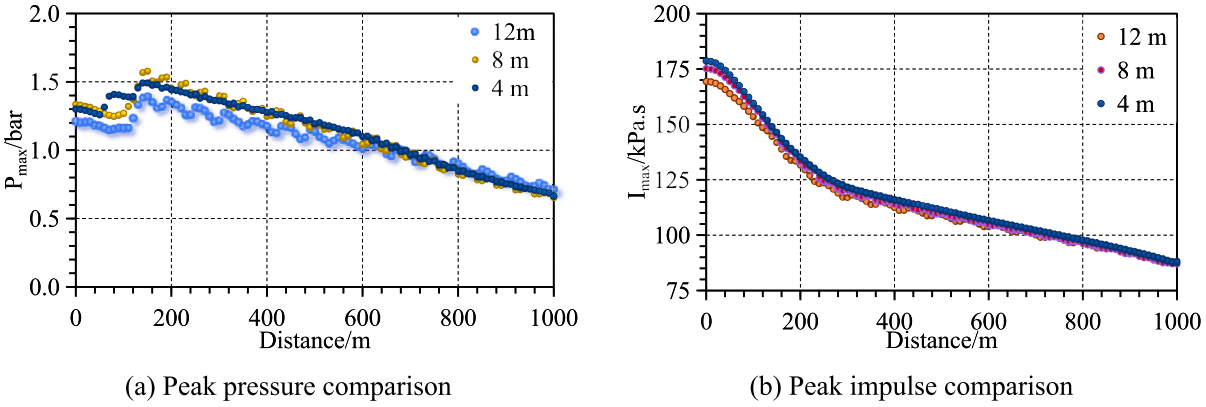

Fig. 14. Peak pressure and impulse comparison with different obstacle distances (BR = 0.06).

scenario, the differences among various obstacle distances were minimal, with peak pressures and impulses closely aligned. Thus, for BR = 0.06, obstacle spacing had a negligible influence on blast loading.

As BR increased to 0.1, the effect of obstacle spacing became more pronounced. Fig. 15 illustrates that when measuring closer to the ignition point, the tunnel with a 12 m obstacle spacing achieved the highest peak pressure and impulse. However, as the measurement location moved farther downstream (e.g., 1000 m from the ignition), blast loading in the 12 m spacing scenario decayed most rapidly, ultimately becoming the lowest at that distance. Conversely, the tunnel with a 4 m obstacle spacing recorded the second-highest peak pressure but the lowest impulse near the ignition point, eventually becoming the highest at 1000 m.

When BR reached 0.2, as presented in Fig. 16, the tunnel with a 12 m obstacle spacing again yielded the highest peak pressure and impulse near the ignition point, but the lowest values at 1000 m. The tunnels with 8 m and 4 m obstacle spacing produced similar peak pressures, although the tunnel with 4 m spacing had the lowest impulse near the ignition and the highest at 1000 m.

These observations differ from the findings of a previous study (Chen, 2023); which suggested that obstacles generally enhance blast loads in gas explosions and that shorter obstacle spacing would produce highest peak pressure. The discrepancy may be attributed to the competing effects of pressure enhancement and energy dissipation.

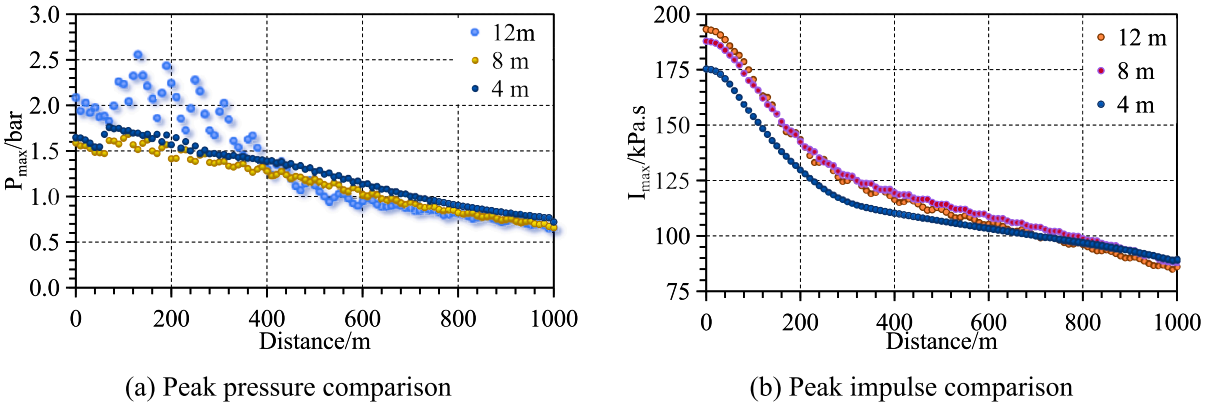

Fig. 15. Peak pressure and impulse comparison with different obstacle distances (BR = 0.1).

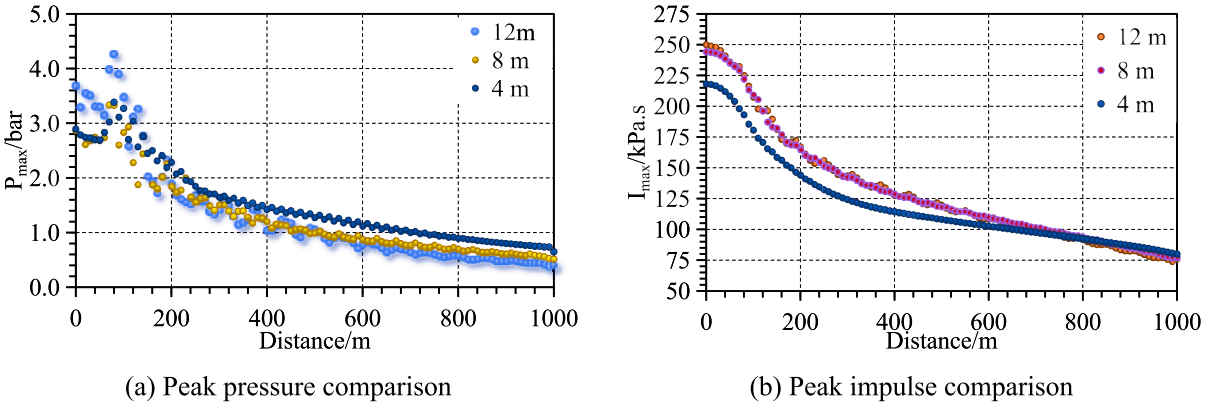

Fig. 16. Peak pressure and impulse comparison with different obstacle distances (BR = 0.2).

Although obstacles intensify turbulence and flame acceleration, thereby increasing localized pressures, they also accelerate energy dissipation within the flow field. As a result, while closely spaced obstacles may initially raise peak pressure levels, they can simultaneously promote faster energy loss, ultimately altering the expected relationship between obstacle spacing and blast load magnitude.

4. Spatio-temporal overpressure prediction

Building on the insights gained from the parametric influence analysis, an efficient predictive tool is required to address the computational demands of detailed numerical simulations. While numerical simulations offer high accuracy, they are often computationally intensive and time-consuming. To improve efficiency, an ANN-based model was developed to estimate blast loading in long, straight tunnels.

According to UFC 3–340 (Structures to resist the effects of accidental explosions, 2008), the negative phase of a shock or pressure wave is typically much weaker and less significant in most scenarios. As a result, it is often disregarded in blast-resistant design, leading to conservative structural solutions. Following this guideline, only the positive phase of the blast loading was considered in this study.

For protective structural design, the design blast loading is typically characterized by the incident blast pressure when the blast wave propagation direction is parallel to structure's surface (Structures to resist the effects of accidental explosions, 2008). In this case, the blast wave propagates along the tunnel axis, and since the walls are parallel to the wave direction, they do not experience reflected pressure. As a result, the predicted pressure on the walls is assumed to be the incident pressure. The critical parameters for the blast wave include the peak pressure P_{so} and peak positive impulse I_0, while the positive phase duration t_d can be calculated by $2I_0/P_{so}$, consistent with the common design simplification of representing the blast loading as a triangular pulse (Design of blast-resistant buildings, 2010).

4.1. Characterization of blast loading in tunnel with obstacles

The relationships among blast loading parameters and distance, tunnel dimensions, fuel amount, obstacles were established in dimensionless form for two primary reasons. First, dimensionless formulation eliminates the influence of scale effects, allowing direct comparison of results across different physical scales. Second, dimensionless parameters significantly reduce the parameter space required for training the ANN model, enabling more efficient model development while maintaining predictive accuracy. This approach allows the model to be readily applied to tunnels of varying sizes and configurations, ensuring its adaptability across a wide range of scenarios and making it a practical tool for predicting blast loads.

The hydraulic diameter (D_h) was utilized to characterize different cross-sectional shapes, which is defined as Eq. (1):

$$D_h = \frac{4A}{P} \tag{1}$$

where A is the cross-sectional area of the flow, m^2; P is the wetted perimeter of the cross-section, m. In the present study, A and P are the inner cross-sectional area and the inner cross-sectional perimeter of the tunnel, respectively.

Then the length-diameter ratio of fuel $\bar{L}$, a widely recognized key factor influencing blast loading magnitude in tunnel-like spaces (Bjerketvedt et al., 1997); is calculated by Eq. (2):

$$\overline{L} = \frac{L_{\text{fuel}}}{D_h} \tag{2}$$

The cross-sectional shape factor S_f is utilized to characterize the shape effect, which was calculated by Eq. (3):

$$S_f = \frac{W}{H} \quad 3$$

The obstacle effect was characterized by blockage ratio (Bjerketvedt et al., 1997), as shown in Eq. (4):

$$BR = \frac{A_{\text{obstalce}}}{A_{\text{tunnel}}} \quad 4)$$

The obstacle distance factor, introduced in this study to quantify the number of obstacles contributing to blast loading, is defined by Eq. (5) (Chen, 2023):

$$BD = \frac{L_{\text{fuel}}}{D_{\text{obstacle}}} \quad 5)$$

Sachs scaling, which converts explosion parameters (pressure, time, distance) into dimensionless forms to enable direct comparison of explosion data under varying energy and environmental conditions, was applied to present the relations among explosion energy and distance, and the dimensionless energy-scaled distance $\overline{R}$ is given by Eq. (6) (van den Berg, 1985):

$$\overline{R} = R(P_0/E_0)^{1/3} \tag{6}$$

where R is the distance from the ignition to the concerned location, m; P_0 is the ambient atmospheric pressure, 10^5 Pa; E_0 is the total combustion energy in the fuel cloud, J, 3.5×10^6 J/m^3 for 9.5 % (V) methane-air mixture at room condition (van den Berg, 1985).

The dimensionless peak overpressure p' is given by Eq. (7):

$$p' = \frac{P_{\text{so}}}{P_0} \quad 7)$$

where P_{so} is the peak overpressure, Pa; P_0 is the ambient pressure, 10^5 Pa.

The dimensionless impulse I' is defined by Eq. (8) (van den Berg, 1985):

$$I' = 2\left[\frac{c_0}{\left(P_0^{2/3}E_0^{1/3}\right)}\right] I_0 \quad 8)$$

where I_0 is the positive phase impulse, Pa.s (Alonso, 2006); c_0 represents the sound of speed, 340 m/s.

4.2. The ANN-based prediction model

According to Eq. (1) to Eq. (8), the objective function of the ANN-based model can be expressed as:

$$(p', I') = f\left(\overline{R}, \overline{L}, S_f, BR, BD\right) \quad 9)$$

ANN was employed to fit the variables and corresponding results. A typical backpropagation neural network, consisting of an input layer, a single hidden layer and one output layer, was adopted. The universal approximation theorem—demonstrating that a single hidden layer is sufficient to approximate any continuous function—supports this configuration; detailed theory can be found in the literature (Li, et al., 2012). Critical parameters for the present study are illustrated below.

The topology of the BP neural network is shown in Fig. 17. The fractions of samples employed for training and testing are 90 % and 10 %, respectively. A systematic analysis was conducted regarding the number of hidden nodes by gradually increasing the node count starting from 4. The analysis revealed that optimal performance was achieved with 16 hidden nodes, as indicated by the minimal MSE and average error; further increases beyond 16 nodes did not yield significant improvements. Thus, the number of hidden neurons was set to 16.

The activation functions used in the hidden layer and output layer are Tansig(x) and Purelin(x), respectively. The network training function is Trainlm (Levenberg-Marquardt backpropagation). The backpropagation neural network is implemented by using the machine learning toolbox in MATLAB R2024b. The maximum training epochs, the training goal and the training rate are 5000, 10^{-5} and 10^{-2}, respectively.

The input and output parameters, alongside their value ranges for

Table 2
Input and output parameters for the ANN model.

Variables		Physical meaning	Range
input	$\overline{R}$	Indicate the fuel amount, distance	0 to 71.5
	$\overline{L}$	Indicate the fuel length, cross-sectional area	1.25 to 25
	S_f	Indicate the croess-sectional shape	0.25 to 4
	BR	Blockage ratio	0.02 to 0.2
	BD	Indicate the obstacle distance	4.17 to 12.5
Output	p'	Peak pressure	0.19 to 4.8
	I'	Impulse at the rising phase	5.4 to 83.1

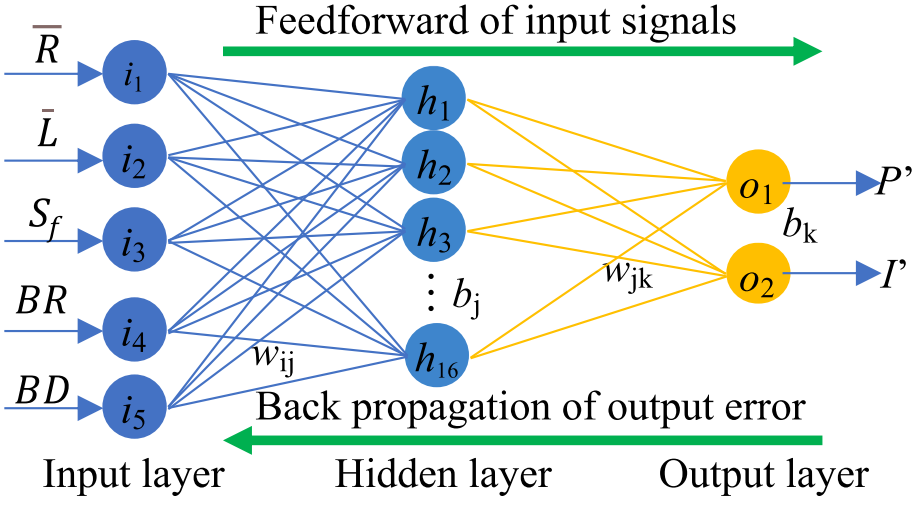

Fig. 17. Structure of the backpropagation neural network.

the ANN-based prediction model are summarised in Table 2. All the input data were generated from the simulations with ignition at closed end. A total of 2525 dataset was used for the ANN training. The training process utilized the Levenberg-Marquardt Backpropagation (trainbr) method, which incorporates built-in regularization mechanisms to help prevent overfitting.

The training performance is illustrated in Fig. 18, which illustrates the model's convergence behavior. Notably, the model achieves its optimal performance after 469 epochs, achieving a Mean Squared Error (MSE) of 0.0014 for the training set and 0.0022 for the testing set. Additionally, the evaluation metrics indicate strong performance, with Mean Absolute Error (MAE) for p' at 0.0597 and Variance Accounted For (VAF) for p' at 0.9569, while MAE for I' is 0.5812 and VAF for I' is 0.9944. Moreover, the close agreement between the training and testing metrics confirms that overfitting has been effectively mitigated.

Fig. 19 compares the numerical and ANN-based results, alongside the relative prediction error. The model demonstrates excellent fitness, with R^2 values exceeding 0.95, and most predicted results falling within a ±30 % error margin. The relative prediction error distribution further shows that 90 % of the predicted points are within a relative error of ±15 % for p' and ±5 % for I', respectively. highlighting the strong predictive performance and reliability of the ANN-based model.

For the convenient use of the trained ANN model, the weights (w_{ij}^{input}, w_{jk}^{hidden}) and biases (b_j^{hidden}, b_k^{output}) of the final ANN model are provided in Table 3, Table 4 and Eq. (10). These parameters represent the connections between the input layer and the hidden layer (w_{ij}^{input}, b_j^{hidden}), and the hidden layer and the output layer (w_{jk}^{hidden}, b_k^{output}). These parameters can be directly utilized to predict the blast loading in long straight tunnels within the data range shown in Table 2.

$$b_j^{\text{hidden}} = \begin{bmatrix} 1.1743 \\ 3.1457 \\ -3.6020 \\ 0.8285 \\ 12.4870 \\ -0.1414 \\ 1.1111 \\ 1.0711 \\ 1.3374 \\ 31.1964 \\ -4.1990 \\ 2.7256 \\ -2.1708 \\ -27.4928 \\ -30.5928 \\ -2.9636 \end{bmatrix} \quad b_k^{\text{output}} = \begin{bmatrix} -5.6080 \\ 0.2881 \end{bmatrix} \tag{10}$$

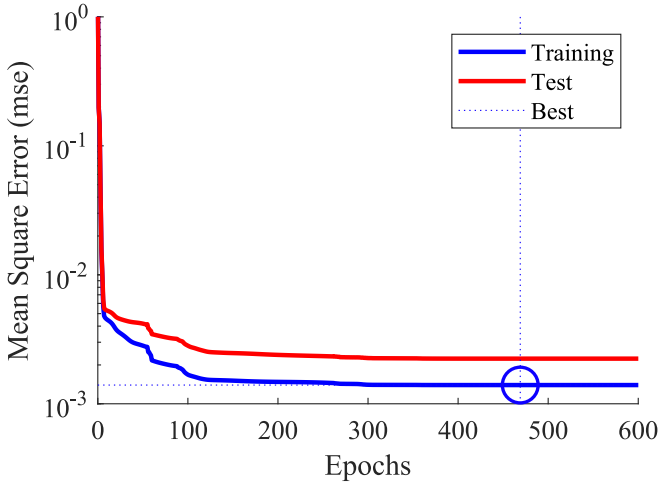

Fig. 18. The convergence curve.

4.3. Validation of proposed model

Experimental data from a large-scale test tunnel in reference (Li et al., 2020) was utilized to validate the proposed ANN-based model. The test tunnel has a cross-sectional area of 7.2 m^2. The total methane-air mixture was 100 m^3 in the experiment with a fuel length (L_{fuel}) of 14 m. The total energy is approximately 333 MJ/J (van den Berg, 1985). The hydraulic diameter (D_{h}) was calculated as 2.816 m based on Eq. (1). The length-diameter ratio of fuel$\overline{L} = L_{\text{fuel}}/D_{\text{h}} = 4.971$. The arc of the tunnel was converted to a rectangular with the same width and area, then $S_f = 1.416$ according to Eq. (3). According to the literature (Li et al., 2020); BR and BD are 0.142 and 14, respectively.

Take the data point at 10 m away as an example, the calculation was demonstrated as the following steps: (1) $\overline{R} = 10 \times (10^5/333/10^6)^{1/3} = 0.67$; (2) Normalize the input data using the formular ($x_{\text{normalized}} = 2.\frac{x-x_{\min}}{x_{\max}-x_{\min}} - 1$), resulting in the following inputs: $\overline{R}_{\text{normalized}} = -0.981$, $\overline{L}_{\text{normalized}} = -0.687$, $S_{\text{f, normalized}} = -0.378$, $BR_{\text{normalized}} = 0.356$, $BD_{\text{normalized}} = 1.360$; (3) The normalized inputs are processed through the trained ANN to calculate the predicted rotation angle. In the first step, the net input to each of the 16 hidden neurons is computed using $z_j = \sum_{i=1}^{5} w_{ij}^{\text{input}} \cdot x_i + b_j^{\text{hidden}}$, where w_{ij}^{input} and b_j^{hidden} are the weights and biases (shown in Table 3 and Eq. (10) connecting the input layer to the hidden layer. The hidden neuron activations are then obtained by applying the Tansig activation function: $h_j = \frac{2}{1+e^{-2z_j}} - 1$. These activations are further processed in the output layer. The net input to the output neuron is calculated as $y = \sum_{j=1}^{8} w_{jk}^{\text{hidden}} \cdot h_j + b_k^{\text{output}}$, using weights and biases w_{jk}^{hidden} and b_k^{output} (shown in Table 4 and Eq. (10) connecting the hidden layer to the output layer. The output layer applies the Purelin activation function $y = \text{purelin}(z) = z$ to produce the normalized peak pressure and impulse; (4) the normalized rotation angle is denormalized to obtain the actual predicted values.

Fig. 19 shows the comparison between experimental and ANN-based results, demonstrating that the model predicts both peak pressure and impulse with a relative error of less than 30 %, validating its effectiveness and reliability. To further compare the overpressure-time history, Fig. 20 and Fig. 21 provide an example of blast loading 10 m from the ignition point. The figure illustrates the overpressure-time curves obtained from experimental data and ANN predictions. While the ANN accurately predicts the peak pressure and duration of the positive phase, it does not capture the oscillatory behavior of the blast wave seen in the experimental data. This limitation is inherent in the ANN's simplification of complex interactions between the flame and its surrounding environment during pressure buildup, but the overall agreement confirms its utility for engineering applications.

5. Conclusion

This study established a dimensionless model for predicting gas blast loading in long, straight tunnels by integrating validated numerical simulations with an ANN-based approach. The dimensionless formulation effectively eliminated scale effects, allowing the model to be readily adapted to tunnels of various sizes and configurations, thus broadening its applicability.

By exploring the effects of ignition position, cross-sectional area and shape, tunnel length, fuel length, blockage ratio, and obstacle spacing, the parametric analyses revealed that these factors strongly influence overpressure and impulse distributions, with non-monotonic trends emerging under certain conditions. Importantly, the results offer practical guidance for safer tunnel design. For example, minimizing the installation of ignition-prone equipment at closed ends, adopting low-profile (short and flat) cross-sectional designs, enhancing ventilation to reduce the effective fuel length, decreasing the number of obstacles, and increasing the spacing between obstacles can all contribute to

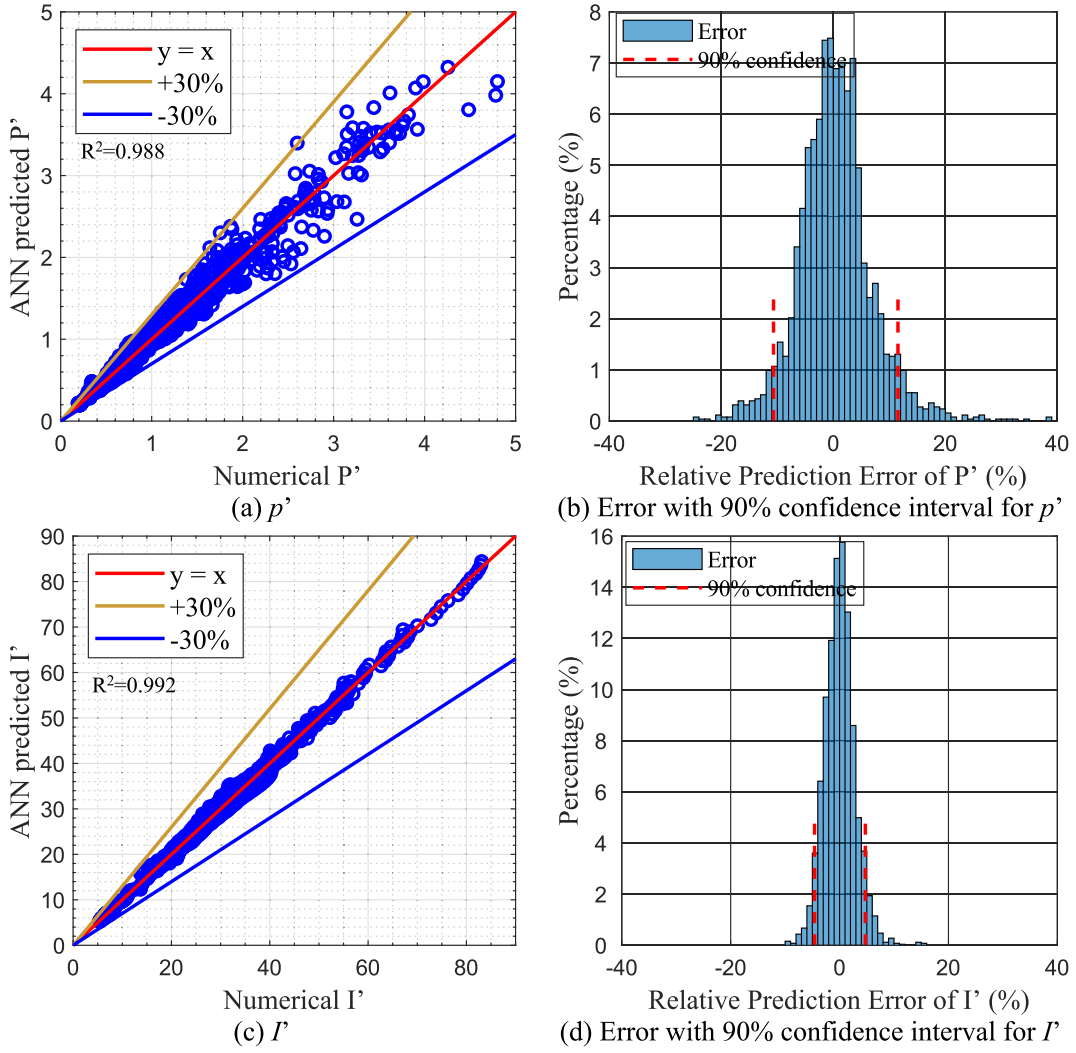

Fig. 19. Comparison between the numerical and ANN-based results and error distribution.

Table 3
Values for w_{ij}^{input}

j / i	1	2	3	4	5
1	2.1730	−0.9346	−0.6888	0.0501	0.0016
2	1.9072	1.2556	−11.0606	−0.7256	5.3665
3	−3.7665	0.3955	0.0735	0.1939	0.0223
4	0.3991	1.1013	−2.6921	−0.2380	−0.1050
5	11.4733	−16.3817	−1.1379	−12.5101	7.5262
6	−0.8860	20.6918	−8.9735	−4.8416	−3.7671
7	1.7424	−1.1994	−1.9731	1.6627	−0.0608
8	2.0044	−0.6879	−0.5832	−0.0112	0.0005
9	0.8266	−1.3971	−2.3538	−0.5632	0.1095
10	25.0639	28.5205	−0.5581	−7.9466	0.9220
11	−4.4357	0.4747	0.0352	0.1560	0.0311
12	−2.2449	1.4415	2.1540	−1.9231	1.1267
13	−1.6776	0.0489	0.0451	0.1688	−0.0002
14	−20.5419	−9.8264	1.2737	9.1185	−1.7059
15	−24.5173	−27.9272	0.3814	7.7383	−0.7773
16	−1.5371	−0.1947	−0.1285	−2.0470	−0.0035

lowering the blast loading.

An ANN-based dimensionless model was proposed and validated to predict the blast loading in long straight tunnel, achieved acceptable agreement compared to numerical results and large-scale test data, maintaining $R2$ values above 0.95 and most predictions within a ±30 % error margin. Over 90 % of the predictions fell within ±15 % for peak pressure and ±5 % for impulse, underscoring the model's accuracy and reliability.

The model can be readily integrated into existing risk assessment frameworks and blast-resistant design for underground facilities,

Table 4
Values for w_{jk}^{hidden}

k j	1	2	3	4	5	6	7	8
1	4.6378	−4.1740	7.3282	1.7874	−0.1336	−0.0916	−0.1426	−6.0470
2	0.5509	−0.2390	−1.4679	2.9768	−0.0169	0.0164	−0.3027	−0.4633
k *j*	9	10	11	12	13	14	15	16
1	3.1531	3.7943	−4.3512	0.1345	−8.7379	0.4359	3.8751	−0.4076
2	−2.5729	0.6368	1.2688	0.0949	1.4214	0.0551	0.6594	−0.3379

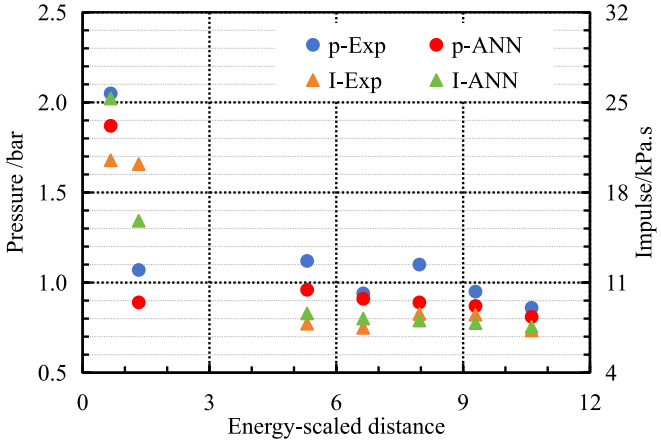

Fig. 20. Comparison of experimental and ANN-Based results.

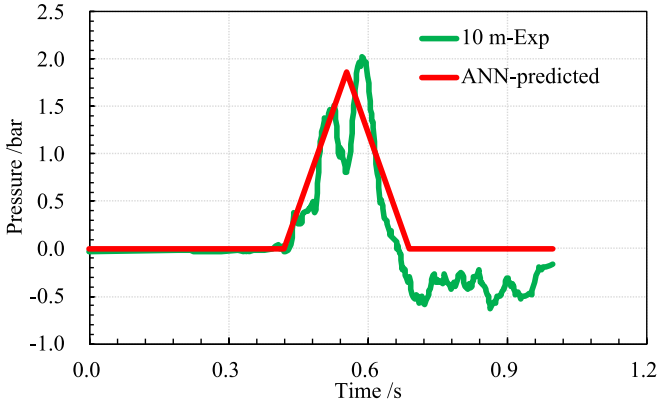

Fig. 21. Comparison of overpressure-time history at 10 *m*.

providing engineers with an efficient tool for evaluating explosion scenarios without resource-intensive CFD simulations. Future work will expand this approach to address complex tunnel geometries, non-homogeneous fuel mixtures, and advanced AI architectures to better capture blast wave behavior, ultimately developing a comprehensive framework for explosion risk assessment in underground infrastructure.

Declaration of Generative AI and AI-assisted technologies in the writing process

Statement: During the preparation of this work the authors used ChatGPT, an AI language model to improve the readability and language of this work. After using this tool, the authors reviewed and edited the content as needed and take full responsibility for the content of the publication.

CRediT authorship contribution statement

Di Chen: Writing – review & editing, Writing – original draft, Visualization, Investigation, Formal analysis, Data curation. **Huaixin Zhang:** Supervision, Resources, Methodology, Conceptualization. **Jun Li:** Writing – review & editing, Supervision, Methodology. **Chengqing Wu:** Writing – review & editing, Supervision, Methodology, Funding acquisition, Conceptualization.

Declaration of competing interest

The authors declare that they have no known competing financial interests or personal relationships that could have appeared to influence the work reported in this paper.

Acknowledgments

This work was supported by the Australia Research Council under ARC Discovery Project DP210101100.

Data availability

Data will be made available on request.

References

Tan, B., et al., 2021. Research on size effect of gas explosion in the roadway. Tunn. Undergr. Space Technol. 112, 103921.
Cheng, R., et al., 2021. A state-of-the-art review of road tunnel subjected to blast loads. Tunn. Undergr. Space Technol. 112, 103911.
Li, P., et al., 2020. Explosion mechanism analysis during tunnel construction in the Zengwen Reservoir. Tunn. Undergr. Space Technol. 97, 103279.
Zhao, Y., et al., 2022. Effects of the length and pressure relief conditions on propagation characteristics of natural gas explosion in utility tunnels. J. Loss Prev. Process Ind. 75, 104679.
Zhang, Q., Ma, Q.J., 2015. Dynamic pressure induced by a methane–air explosion in a coal mine. Process Saf. Environ. Prot. 93, 233–239.
Chen, H., Qi, H., Feng, Q., 2013. Characteristics of direct causes and human factors in major gas explosion accidents in chinese coal mines: Case study spanning the years 1980–2010. J. Loss Prev. Process Ind. 26 (1), 38–44.
Li, Z., et al., 2018. Numerical Investigation of the Dynamic responses and damage of Linings Subjected to Violent Gas explosions inside Highway Tunnels. Shock Vib. 2018, 1–20.
Uystepruyst, D., Monnoyer, F., 2015. A numerical study of the evolution of the blast wave shape in rectangular tunnels. J. Loss Prev. Process Ind. 34, 225–231.
Chen, D., et al., 2024. A full-scale experimental investigation of natural gas explosion in a 710-m long utility tunnel with multiple pipelines. Tunn. Undergr. Space Technol. 153, 106049.
Chen, D., Wu, C., Li, J., 2023. Assessment of modeling methods for predicting load resulting from hydrogen-air detonation. Process Saf. Environ. Prot. 180, 752–765.
Chen, D., et al., 2024. A generic approach for modelling hydrogen-methane-air detonation in hydrocode. J. Clean. Prod. 465, 142840.
Hernandez, F., et al., 2024. Analysis of fuel storage tanks under internal deflagrations with different venting technologies: an experimental and numerical study. Eng. Fail. Anal., 108948
Chen, D., et al., 2023. 【】 pressure-time history model of methane-air explosion in tunnel-shape space. J. Loss Prev. Process Ind. 82, 105004.
Chen, D., Wu, C., Li, J., 2025. A fast and reliable model for predicting hydrogen-methane-air blast loading in unconfined spaces for blast-resistant design. Int. J. Hydrogen Energy 97, 1316–1326.
Zhang, Z., et al., 2023. Spatial distribution and machine learning-based prediction model of natural gas explosion loads in a utility tunnel. Tunn. Undergr. Space Technol. 140, 105272.
van den Berg, A.C., 1985. The multi-energy method: a framework for vapour cloud explosion blast prediction. J. Hazard. Mater. 12 (1), 1–10.

Xu, Q., et al., 2023. Prediction of venting gas explosion overpressure based on a combination of explosive theory and machine learning. Expert Syst. Appl. 234, 121044.
Grégoire, Y., et al., 2022. Vented gas explosion overpressure calculation based on a multi-layered neural network. J. Loss Prev. Process Ind. 74, 104641.
Chen, D., et al., 2022. A numerical study of gas explosion with progressive venting in a utility tunnel. Process Saf. Environ. Prot. 162, 1124–1138.
GEXCON, FLACS v10.9 User's Manual. 2019.
Hansen, O.R., Johnson, D.M., 2015. Improved far-field blast predictions from fast deflagrations, DDTs and detonations of vapour clouds using FLACS CFD. J. Loss Prev. Process Ind. 35, 293–306.
Bjerketvedt, D., Bakke, J.R., van Wingerden, K., 1997. Gas explosion handbook. J. Hazard. Mater. 52 (1), 1–150.
Xu, Y., Huang, Y., Ma, G., 2020. A review on effects of different factors on gas explosions in underground structures. Underground Space 5 (4), 298–314.
Zhu, Y., et al., 2020. Investigation on the overpressure of methane-air mixture gas explosions in straight large-scale tunnels. Process Saf. Environ. Prot. 135, 101–112.
Structures to resist the effects of accidental explosions, in UFC 3-340-02. 2008, Department Of Defense: Unites States of America. p. 1-1943.
[26] Design of blast-resistant buildings in petrochemical facilities. 2010, American Society Of Civil Engineers: the United States of America. p. 1-311.
Alonso, F.D., et al., 2006. Characteristic overpressure–impulse–distance curves for vapour cloud explosions using the TNO Multi-Energy model. J. Hazard. Mater. 137 (2), 734–741.
Li, J., et al., Brief Introduction of Back Propagation (BP) Neural Network Algorithm and Its Improvement. 2012, Springer Berlin Heidelberg: Berlin, Heidelberg. p. 553-558.
Li, R., Si, R., Wang, L., 2020. Propagation of gas explosions of different volumes in a large test tunnel. Energy sources. Part a, Recovery, Utilization, and Environmental Effects 1–13.